

This is a self-archived – parallel published version of this article in the publication archive of the Gonbad Kavous University (Archived by **Dr. Mohammad Farshad**, Email: [farshad \[at\] gonbad.ac.ir](mailto:farshad@gonbad.ac.ir)). It might differ from the original.

Version: Accepted article

Copyright ©2021 IEEE. Personal use of this material is permitted. Permission from IEEE must be obtained for all other uses, in any current or future media, including reprinting/republishing this material for advertising or promotional purposes, creating new collective works, for resale or redistribution to servers or lists, or reuse of any copyrighted component of this work in other works.

Please cite the original version:

M. Farshad, "Fault Location in HVDC Grids Equipped With Quick-Action Protections and Circuit Breakers Based on Voltage Transient Response," in *IEEE Transactions on Industrial Electronics*, vol. 68, no. 12, pp. 12881-12889, Dec. 2021, doi: 10.1109/TIE.2020.3044815.

Fault Location in HVDC Grids Equipped with Quick-Action Protections and Circuit Breakers Based on Voltage Transient Response

Mohammad Farshad

Abstract-- A novel fault-location scheme is designed for transmission lines of high-voltage dc (HVDC) grids equipped with quick-action protections and circuit breakers using very few milliseconds of postfault signals, measurable before the ultra-fast fault-isolation stage. A simplified equivalent circuit analysis shows that the first negative overshoot time and average derivative of voltage in the early postfault moments are directly related to the fault location. However, due to HVDC grids' characteristics and several factors involved in reality, the analytical use of these features may not be feasible or may not result in an acceptable accuracy. Hence, a soft computing strategy is adopted to overcome this problem. Based on this strategy, machine-learning-based locators are trained for both line terminals, each responsible for locating faults in the half-line of its side using the two introduced features extracted from the locally captured voltage signals. The statistical evaluations of the performance on a 4-terminal grid for various fault cases not considered in the training stage confirm the designed scheme's satisfactory accuracy, generalization ability, tolerance to noisy measurements, and tolerance to changes in the line parameters.

Index Terms-- Fault location, feature extraction, HVDC transmission, transient response, voltage-source converters.

I. INTRODUCTION

OVER the last few years, high-voltage dc (HVDC) grids based on voltage-source converters (VSCs) have attracted much attention, especially for transmitting the electrical energy produced from remote renewable resources [1]. As with any transmission system, the location of line faults in these grids should be accurately determined so that the repair crew can perform corrective operations in the shortest possible time to decrease the faulted line's outage time. It should be noted that some types of VSCs cannot handle fault currents. HVDC grids based on such converters are usually equipped with ultra-high-speed protections and hybrid dc circuit breakers (HDCBs) [2] to quickly detect and isolate faulty sections within few milliseconds and prevent the entire outage. In such grids,

minimal postfault data measurable before the fault-isolation stage makes it challenging to design an accurate fault locator.

To date, some exemplary methods have been presented for fault location in two-terminal VSC-HVDC systems based on combinations of theories and techniques, e.g., the traveling-wave theory, wavelet transform, and the generalized logistic function fitting technique in [3], the modal and traveling-wave theories in [4], the traveling-wave theory and injection of pulses via converters in [5], the traveling-wave theory and change detection in double-end transient currents in [6], and the traveling-wave theory and time-frequency data extraction in [7]. However, the applicability of these methods to multiterminal grids needs more investigations and analyses [4].

There are also valuable fault-location methods that have been explicitly provided for and tested on multiterminal VSC-HVDC systems. The authors in [8]-[12] have proposed methods based on the traveling-wave theory and the continuous wavelet transform. The methods presented in [8]-[10] require synchronized current signals sampled at converter stations with a frequency in the MHz range. Despite a lower sampling frequency requirement of the ones proposed in [11], [12], they need synchronized current signals captured through sensors distributed along transmission lines. The authors in [13] have designed a fault locator based on the high-frequency components and electromagnetic time-reversal of synchronously measured currents from both line terminals. However, in [13], it has been assumed that slow ac-side circuit breakers isolate dc line faults, and accordingly, relatively wide data windows from postfault signals have been used for locating dc line faults. The authors in [14] have suggested a fault-location method based on the high-frequency components and fast Fourier transform of current signals captured from both line-ends. The method suggested in [14] also seems unsuitable for the grids with quick-action protections and dc-side circuit breakers due to its required relatively wide data windows from postfault signals. In [15], the authors have designed a fault-location scheme based on the simplified R-L model of overhead lines. However, the scheme presented in [15], while requiring synchronized voltage and current signals captured from both

This work was supported by the Gonbad Kavous University (Project ID: 6-484).

M. Farshad is with the Department of Electrical Engineering, Faculty of Basic Sciences and Engineering, Gonbad Kavous University, Gonbad Kavous 49717-99151, Iran (e-mail: farshad@gonbad.ac.ir).

line terminals, may not be suitable for long overhead or cable lines due to neglecting the shunt capacitance in the line model. In [16], the authors have designed a valuable scheme employing the dynamic line model estimation and gradient descent algorithms. The scheme presented in [16] also requires synchronized voltage and current signals captured from both line terminals and neglects lines' frequency-dependent parameters. The authors in [17] have presented an innovative method based on the velocity difference of current modal components in cable-layers. However, the method designed in [17] requires a relatively high sampling frequency in the MHz range, and its accuracy needs to be improved for resistive faults.

This article mainly focuses on fault location in multiterminal VSC-HVDC grids equipped with quick-action protections and circuit breakers. At first, a simplified equivalent circuit is analyzed to introduce two useful features for fault location. However, due to HVDC grids' characteristics and multiple factors involved in reality, the analytical use of these features may not be practicable or associated with acceptable accuracy. Hence, a new soft computing-based scheme with an implementable feature-extraction procedure is designed to benefit from the introduced useful features for fault location in real grids. In this scheme, two fault locators are set at both line terminals, each with the task of independently locating faults in its half-line using only the local voltage measurement. Indeed, although there will be a need to synchronize the voltage measurements to determine the faulty half-line and select the appropriate result from the two estimations provided by the two locators, the fault location estimated by each locator is immune to time synchronization errors and communication link disturbances. The sampling frequency required for the designed algorithm is also lower than for the conventional traveling-wave-based methods. Moreover, the proposed algorithm needs a very short data window from the postfault voltage signal. This advantage ensures the availability of its required data before the isolation of permanent or nonpermanent faults in the grids with ultra-high-speed protections and HDCCBs.

The next sections of this article are arranged as follows: In Section II, short-circuit faults in a transmission line connected to a single converter are analyzed, and useful features are selected for fault location. In Section III, the feature-extraction procedure is described for real systems, and the behaviors of the selected features are investigated in a multiterminal grid. The designed fault-location scheme is depicted in Section IV. The evaluation results are also given in Section V. Ultimately, this article is concluded in Section VI.

II. FAULTS IN A LINE CONNECTED TO A SINGLE CONVERTER

The half-bridge modular multilevel converter (HB-MMC), notwithstanding its inability to control fault currents, is one of the main options for multiterminal grids owing to its lower cost and losses and higher flexibility than other types of VSCs [18]. This converter type has been utilized in real projects such as *Nanao*, *Zhoushan*, and *Zhangbei* [18], [19]. Hence, this article's studies have also been performed with specific consideration given to this converter type.

Fig. 1 illustrates an HB-MMC in the event of a positive-to-

ground (p-g) fault in the line connected to it, in the early postfault moments before the fault isolation or the converter blocking [20]. The natural point grounding resistance of the three-phase star-connected source, R_g , is assumed to be zero to provide a lower resistance path for the p-g fault current. In this figure, x indicates the distance between the terminal and the fault point, R_f is the fault resistance, L_{lim} is the inductance of the HDCCB's current limiter, C_m denotes the capacitance of each converter submodule (SM), N indicates the number of SMs in each converter arm, R_a is the resistance of each converter arm, L_a is the inductance of each converter arm, V_f is the prefault pole-to-ground voltage at the fault point, V_p denotes the measured voltage of the faulty pole at the terminal, and V_{fp} stands for the superimposed voltage of the faulty pole at the terminal. Although the total number of inserted SMs from the upper and lower arms of each converter leg is equal to N at any time of regular operation, each arm's share varies with time (in the range of 0 to N). If an average of $N/2$ inserted SMs is considered for each arm [20], each arm's equivalent capacitance will be $2C_m/N$. Therefore, each converter arm's impedance in the s-domain will be equal to $sL_a + R_a + N/(2sC_m)$. When the ac-side voltage sources are short-circuited based on the superposition theorem, the parallel impedances of the three converter arms can be replaced by an equivalent impedance of $sL_a/3 + R_a/3 + N/(6sC_m)$. Thus, the simplified equivalent circuit in the s-domain is obtained, as shown in Fig. 1, considering only the fault effects.

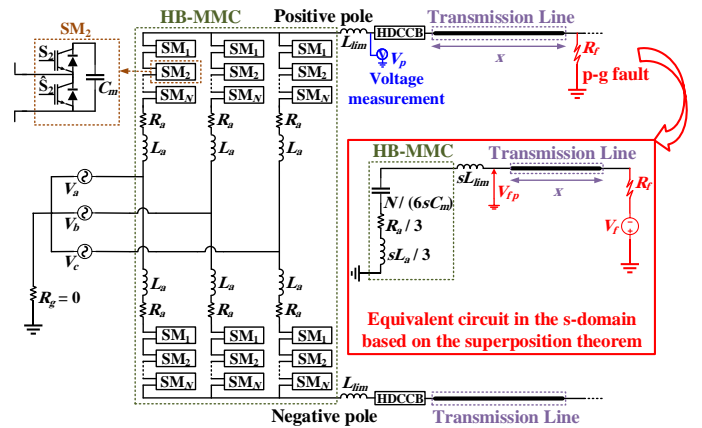


Fig. 1. Equivalent circuit of an HB-MMC with an ideal three-phase star-connected source in the early moments after a p-g line fault.

A. Transmission Line with R-L Model

If the transmission line of Fig. 1 is modeled by the series lumped R-L elements [15], ignoring the shunt capacitance, the obtained equivalent circuit will be a second-order circuit. Considering V_f and V_{fp} as the input and output variables, respectively, the transfer function of this second-order circuit, $H(s)$, is obtained as follows:

$$H(s) = \frac{V_{fp}}{V_f} = -\frac{k_2 \omega_n^2 s^2 + k_1 \omega_n^2 s + k_0 \omega_n^2}{s^2 + 2\xi \omega_n s + \omega_n^2} \quad (1)$$

where, k_0 , k_1 , and k_2 are the constant gain coefficients. Also, ω_n

and ξ are the undamped natural angular frequency and the damping factor, respectively. These parameters can be calculated as follows:

$$k_0 = 1, \quad k_1 = \frac{2C_m R_a}{N}, \quad k_2 = \frac{2C_m L_a + 6C_m L_{lim}}{N} \quad (2)$$

$$\omega_n = \sqrt{\frac{N}{2C_m L_a + 6C_m L_{lim} + 6C_m x L_L}} \quad (3)$$

$$\xi = \left(\frac{R_a}{6} + \frac{x R_L}{2} + \frac{R_f}{2} \right) \sqrt{\frac{18C_m}{N L_a + 3N L_{lim} + 3N x L_L}} \quad (4)$$

where, L_L and R_L are the inductance and resistance per unit length of the line. Given the typical values for the converter's resistance, inductance, and capacitance, the values of k_1 and k_2 will be in the range of 10^{-5} and much smaller than k_0 with the value of 1. Therefore, (1) can be approximated as follows:

$$H(s) = \frac{V_{fp}}{V_f} \cong -\frac{\omega_n^2}{s^2 + 2\xi\omega_n s + \omega_n^2} \quad (5)$$

The second-order circuit will have an underdamped step response if the damping factor, ξ , is in the range of (0,1). Table I presents typical specifications for an HB-MMC [21] and a transmission line [15]. Given these specifications and based on (4), for a fault at the distance of 10 km, a fault resistance smaller than 66 Ω , and for a fault at the distance of 100 km, a fault resistance smaller than 81 Ω will result in an underdamped response. The unit-step response for a p-g fault with a 35- Ω resistance at the distance of 100 km from the converter is shown in Fig. 2. In this figure, the first negative overshoot time and the delay time until the step-response reaches half the final value (i.e., -0.5) are indicated as t_{fno} and t_d , respectively. Based on (5), these parameters can also be obtained as follows [22]:

$$t_{fno} = \frac{\pi}{\omega_n \sqrt{1 - \xi^2}} \quad (6)$$

$$t_d \cong \frac{1.1 + 0.125\xi + 0.469\xi^2}{\omega_n} \quad (7)$$

Based on (7), the voltage slope in the early postfault moments, d_{evs} , can be approximately calculated as follows:

$$d_{evs} = \frac{\Delta V_{fp}}{\Delta t} = \frac{-0.5}{t_d} \cong \frac{-0.5\omega_n}{1.1 + 0.125\xi + 0.469\xi^2} \quad (8)$$

If the parameters of the equivalent circuit are known, according to (3) and (4), ω_n will be a function of x , and ξ will be a function of x and R_f . Consequently, according to (6) and (8), t_{fno} and d_{evs} will be functions of x and R_f , i.e., $t_{fno}=f_1(x, R_f)$ and $d_{evs}=f_2(x, R_f)$. Therefore, the simultaneous use of these two features can help to determine the unknown values of x and R_f .

TABLE I
TYPICAL SPECIFICATIONS FOR A CONVERTER AND A TRANSMISSION LINE

| HB-MMC parameters [21] | | | | | Line parameters [15] | |
|------------------------|------------|------------|--------------------|----------------|----------------------|-----------------------|
| N | C_m (mF) | L_a (mH) | R_a (Ω) | L_{lim} (mH) | L_L (mH/km) | R_L (Ω /km) |
| 400 | 11.72 | 84.8 | 0.885 | 150 | 1.3 | 0.0336 |

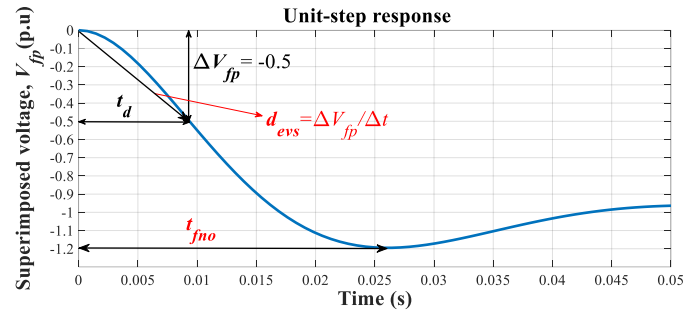


Fig. 2. Unit-step response for a p-g fault with a 35- Ω resistance at the distance of 100 km, considering the R-L line model.

HB-MMC-HVDC grids are usually protected by ultra-high-speed fault detectors and HDCCBs to cover the converters' inability to handle fault currents [2]. Fault detection in less than 1 ms can be possible by employing single-ended protection algorithms designed for HB-MMC-HVDC grids [19], [23]. Also, in an HDCCB, the main breaker based on semiconductor switches is paralleled with a branch, including the load commutation switch (LCS) and the ultra-fast disconnecter (UFD). Under normal operating conditions, the load current passes through this parallel branch. If the HDCCB receives the trip command, the LCS and the UFD open within about 2 ms [2], and the main breaker starts to interrupt the current transferred to its branch. Therefore, assuming a minimum delay of 0.5 ms for the fault-detection stage, the postfault data will be reliably available up to 2.5 ms after the fault signature appearance at the terminal. The studies performed in [24] also confirm the reasonability of the minimum time delay of 2.5 ms, from the fault signature appearance time to when the HDCCB's main breaker starts to open. As shown in Fig. 2, if the simplified R-L line model is used, t_{fno} occurs over a relatively long time, about 26 ms in this example, and requires a relatively wider postfault data window to be extracted. Therefore, even if the converter blocking stage is omitted, and the model is assumed to be valid during this long time, it will not be feasible to use (6) and (8) to locate faults in HB-MMC-HVDC grids due to the quick-action fault detectors and HDCCBs.

B. Transmission Line with Frequency-Dependent Model

If the distributed frequency-dependent line model is considered in the equivalent circuit of Fig. 1, then the transfer function, $H(s)$, will be irrational [23], and it will be so complex to obtain closed-form equations like (6) and (8). Indeed, numerical simulation is the simplest way to get the step response for this circuit. Hence, the equivalent circuit of Fig. 1 is simulated in PSCAD/EMTDC, considering the converter specifications given in Table I and a cable line with the distributed frequency-dependent model and the arrangement

depicted in Fig. 3. Fig. 4 presents the unit-step response of this circuit for a p-g fault with a 35-Ω resistance at the distance of 100 km from the converter. As shown in this figure, the step response has faster oscillating components, in addition to a component similar to the second-order response of Fig. 2. Therefore, the two introduced features (i.e., t_{fno} and d_{evs}) can be desirably extracted within a very short time, in this example, about 0.6 ms after the fault signature appearance at the terminal.

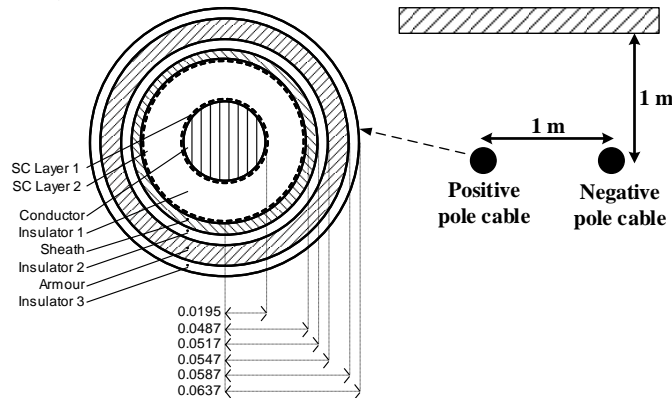


Fig. 3. Configuration of the cable line simulated in PSCAD/EMTDC.

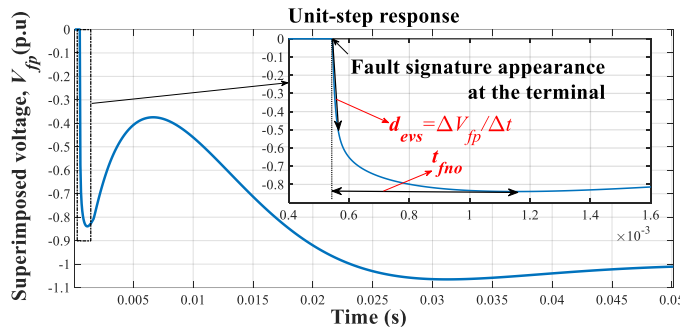


Fig. 4. Unit-step response for a p-g fault with a 35-Ω resistance at the distance of 100 km, considering the frequency-dependent line model.

C. Motivations for Adopting a Soft Computing Strategy

In Section II.A, considering some simplifications, it has been proved that the two introduced features (i.e., t_{fno} and d_{evs}) have valuable relationships with the unknown fault distance and resistance parameters. Also, in Section II.B, it has been shown that these features can be extracted within a very short time in the case of using the exact line model, compatibly with quick-action fault detectors and HDCCBs. However, the following complexities motivate to adopt a soft computing strategy for benefiting from these useful features:

- It is arduous to obtain closed-form equations like (6) and (8) when using the exact line model with the distributed capacitance due to the irrational transfer function [23].
- Fault current paths can be different depending on the implemented grounding scheme [25], [26]. However, the capacitance distributed along faulty and healthy lines is one of the main paths in all the grounding schemes, which will make the relations more complicated.

- The simplified R-L-C model of MMCs may not accurately reflect their behaviors during faults since it does not consider the control dynamics. A more accurate model will also increase the complexity level.
- There is more than one converter/line in a grid, which will make the relations more complicated.
- In real systems, the exact times of fault inception and fault signature appearance at the terminal are usually unknown. Hence, the values of the introduced features should be approximately estimated based on the voltage response around the instant of the line protection trip.

III. FEATURE EXTRACTION IN REAL SYSTEMS

As mentioned in Section II.C, the introduced features should be approximately estimated from measurable signals around the instant of the line protection trip since the exact times of fault inception and fault signature appearance at the terminal are commonly unknown. Therefore, it is vital to design an implementable feature-extraction procedure for real systems.

A. Feature-Extraction Procedure

Although the two introduced features (i.e., t_{fno} and d_{evs}) were extracted from the superimposed voltage in Section II, they can also be extracted directly from the measured voltage; because the peak time and the response slope do not change by adding the prefault value to the response. The following steps are performed to approximately estimate and extract these two features from the measured voltage of the faulty pole, after fault detection by the designated line protection:

- 1) A buffered window of timestamped voltage samples around the fault-detection instant, $V_p[t_{w1}:t_{w2}]$, is considered as the input data. This data window should contain at least 0.1 ms before and 2.5 ms after the appearance of fault signatures at the terminal. The required length of postfault data is compatible with the minimum delay expressed in the last paragraph of Section II.A for fault detection and to start current interruption. If the buffered data window is wider than the mentioned range limits, there will be no problem. Therefore, these range limits can be easily met considering the minimum and maximum detection delay of the designated line protection.

- 2) If the voltage samples are related to the negative pole, then their values are multiplied by -1.

- 3) The buffered data window, $V_p[t_{w1}:t_{w2}]$, is smoothed employing a moving average window, for example, with a length of 60 μs, to reduce the effects of measurement noises and small fluctuations. Functions like *smooth(.)* in MATLAB [27] can be used for this purpose. At any time t , the moving average window with the length of 60 μs performs as follows:

$$V_{psm}[t] = \overline{V_p[t - 30 \times 10^{-6}; t + 30 \times 10^{-6}]} \quad (9)$$

where, V_{psm} contains the smoothed data window of voltage samples. Also, the average operator is indicated by an overbar. For the samples at the beginning and end of the data window, the average window is narrowed as far as samples exist. When

choosing the moving average window's length, a balance should be struck between accuracy and noise tolerance.

4) The average of prefault voltage samples, v_{pre} , is calculated over the first 0.1 ms of V_{psm} :

$$v_{pre} = \overline{V_{psm}[t_{w1}:t_{w1} + 0.1 \times 10^{-3}]} \quad (10)$$

5) The first sample with at least a 5% drop compared to v_{pre} is found in V_{psm} , and the corresponding timestamp is stored as an estimation of the fault signature appearance time, t_0 .

6) The first feature, t_{fno} , is extracted by finding the first negative peak time in V_{psm} and subtracting t_0 from it. Functions like *findpeaks*(.) in MATLAB [27] can easily find signal peaks.

7) The second feature, d_{evs} , is estimated by averaging the numerical derivatives of consecutive samples in V_{psm} from t_0 up to a short time, for example, 60 μ s, after that.

B. Feature Analysis in a Multiterminal Grid

Here, the behaviors of the two introduced features (i.e., t_{fno} and d_{evs}) are analyzed in a test grid. To this end, a ± 320 -kV symmetrical monopolar HB-MMC-HVDC grid with the single-line diagram depicted in Fig.5 is simulated in PSCAD/EMTDC, considering the exact models for its components [21]. The HB-MMCs are accurately simulated using the continuous model with an internal control scheme based on the stored energy estimation [21]. The distributed frequency-dependent model is also considered for its cable lines, with the same arrangement depicted in Fig. 3. In this grid, L_{lim} equals 150 mH for each HDCCB, and the sampling frequency is 250 kHz. The implemented grounding scheme is illustrated in Fig. 6. According to [26], the parallel capacitor used in this grounding scheme, C_g , can be small for MMCs, e.g., in the test grid, $C_g=2.5$ μ F. Other details of this test grid are available in [21].

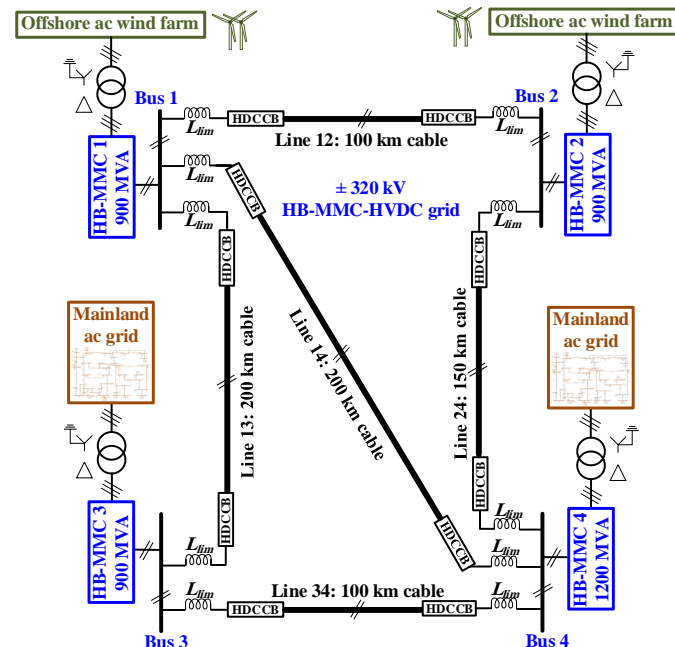


Fig. 5. HB-MMC-HVDC test grid.

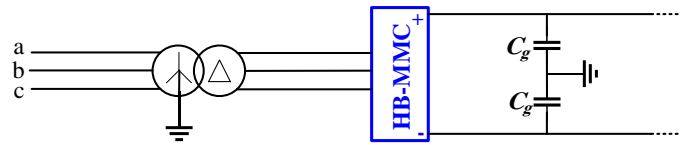


Fig. 6. The grounding scheme implemented in the test grid.

Fig. 7 exhibits variations of the two features (i.e., t_{fno} and d_{evs}) extracted from the faulty pole voltage measured at Bus 1, considering different p-g fault locations and resistances in Line 12. As can be understood from this figure, t_{fno} is more sensitive to changes in the fault location, while d_{evs} is more sensitive to the fault resistance changes. Therefore, the combination of these features in a soft computing-based fault-location scheme can improve the estimation accuracy. However, the irregularity of t_{fno} variations for resistive faults in the second half of the line is an important point comprehensible from Fig. 7(a). Indeed, in the case of resistive faults before the midpoint, the first negative overshoot occurs before any interferences from the multiple reflected and refracted traveling waves between the fault point and the remote terminal. In contrast, for resistive faults after the midpoint, one or more of the traveling waves reflected from the remote terminal may arrive sooner and distort the measured voltage waveform before the first negative overshoot occurrence considering only the circuit between the measuring terminal and the fault point. For solid faults, the reflected waves from the remote terminal will not enter the circuit between the measuring terminal and the fault point. Therefore, as also comprehensible from Fig. 7(a), the variation of t_{fno} will be regular for solid faults at any location along the line.

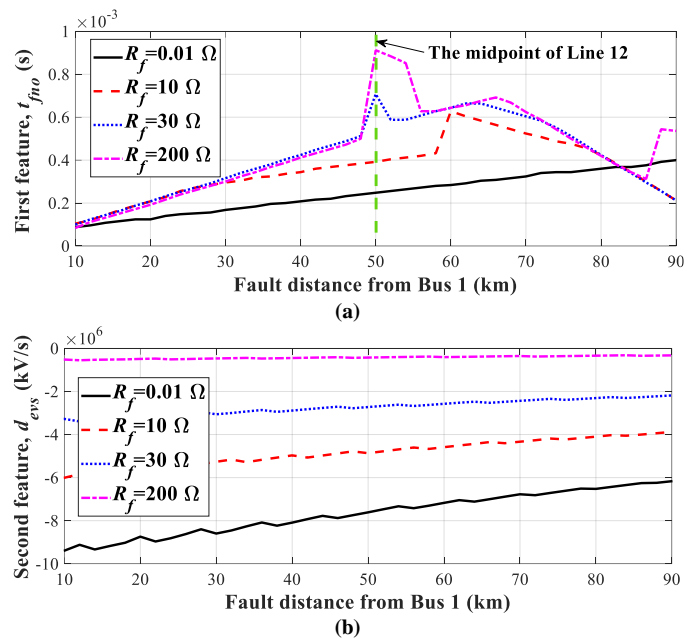


Fig. 7. Variations of the two features extracted from the faulty pole voltage measured at Bus 1, for different p-g fault locations and resistances in Line 12 of the test grid: (a) t_{fno} , (b) d_{evs} .

Fig. 8 represents the voltage signals measured at the positive pole of Bus 1 and their first negative overshoots, considering resistive and solid p-g faults at 0.8 s before and after the midpoint of Line 12. This figure also confirms the above explanation about the possible interferences of reflected traveling waves and their effects on t_{fno} . Based on this analysis, it can be concluded that t_{fno} will only be useful for locating faults in the half-line closer to the measurement point.

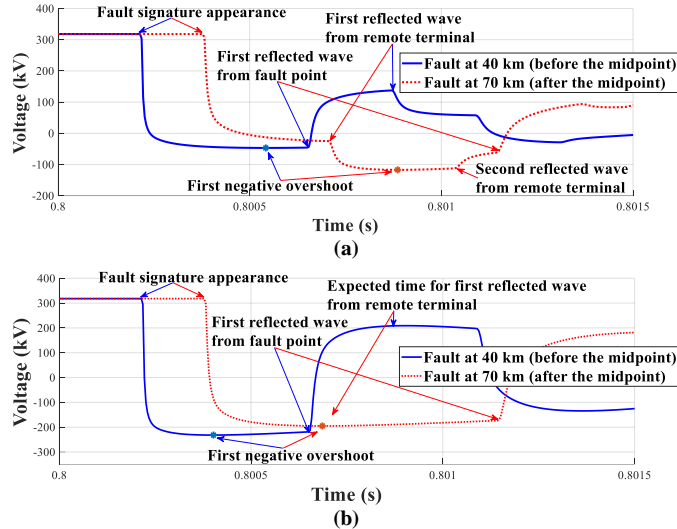


Fig. 8. Voltage signals measured at the positive pole of Bus 1 for p-g faults in Line 12 at the distances of 40 and 70 km from Bus 1: (a) with the fault resistance of 10 Ω , and (b) with the fault resistance of 0.01 Ω .

IV. PROPOSED FAULT-LOCATION ALGORITHM

Since this study focuses on the fault-location scheme, and the fault-detection scheme is beyond its scope, it is assumed that the designated ultra-high-speed line protection can quickly and correctly detect the faulty pole(s). Fig. 9 illustrates the flowchart of the proposed fault-location algorithm. As shown in this flowchart, whenever the relevant protection detects a line fault, the recommended features (i.e., t_{fno} and d_{evs}) are extracted from the faulty pole's locally measured voltage, according to the steps stated in Section III.A. Then, these extracted features are standardized as follows before being presented to a fault-location estimator pretrained using the training patterns:

$$F' = \frac{F - \mu_F}{\sigma_F} \quad (11)$$

where, F and F' are, respectively, the initial and standardized values of an input feature (i.e., t_{fno} or d_{evs}). Also, μ_F and σ_F denote the mean and standard deviation of the corresponding feature in the training dataset, respectively.

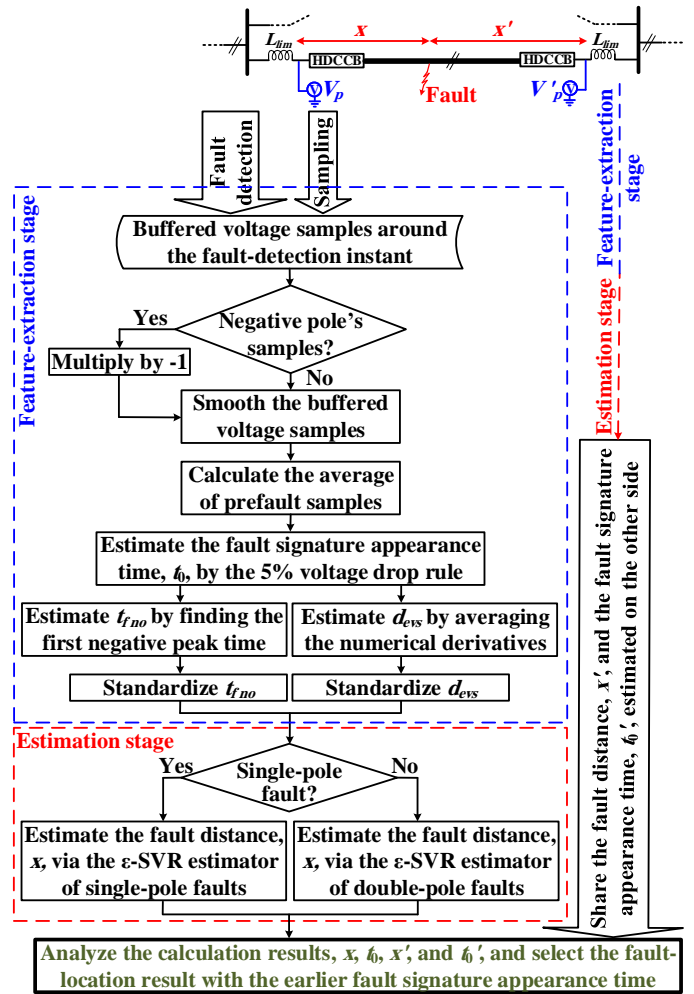


Fig. 9. Flowchart of the designed fault-location algorithm.

The recommended estimator in the designed fault-location algorithm is the well-known ϵ -support vector regression (ϵ -SVR) with the Gaussian kernel function [28]. ϵ -SVR, as an extended version of the binary support vector machine classifier, has strong generalization power. This estimator's parameters include the margin, ϵ_{svr} , box constraint, C_{svr} , and the kernel scale, σ_{svr} . These parameters can be adjusted in the training stage using the k-fold cross-validation and Bayesian optimization techniques [27].

Based on the analysis performed in Section III.B, to accurately locate a fault in a line using the recommended input features, it is necessary to consider independent single-ended fault locators at both terminals of that line, each responsible for locating faults in the half-line of its side. The valid fault-location result will be selected among the two estimated ones by determining the faulty half-line. The faulty half-line can be determined by comparing the fault signature appearance time estimated at both terminals. The earlier signature appearance at any terminal means that the fault is closer to that terminal. Therefore, despite estimating the fault location based on the locally measured voltage at each terminal, the voltage samples should be timestamped synchronously at both terminals to make the time comparison and the faulty half-line determination

possible. A reasonable synchronization error level will only be problematic in determining the half-line for faults very close to the line's midpoint. The effect of these synchronization errors can be diminished by a partial overlap of the area covered by the two locators during their training processes. In the worst case, without time synchronization, two fault-location results will be available, one of which will be accurate.

Although the analyses of Sections II and III are also valid for double-pole faults, the exact values of t_{fno} and d_{evs} for these faults can differ from those extracted for single-pole faults due to the different fault path. Therefore, separate estimators are trained and utilized for single-pole and double-pole faults in each terminal's fault-location algorithm. In the case of double-pole faults, the features are derived using the voltage measured at one of the faulty poles.

V. RESULTS AND DISCUSSION

The presented fault-location scheme is evaluated in the test grid introduced in Section III.B, i.e., in the grid of Fig. 5.

A. Training and Test Datasets

For generating the training dataset, 1980 various fault cases are simulated, considering p-g and positive-to-negative (p-n) faults with the resistances of 0.01, 5, 10, 15, 20, 25, 30, 50, 100, and 200 Ω , and with the locations ranged from 1% up to 99% of Line 14 with a 1% step. For each training fault case, the two input features (i.e., t_{fno} and d_{evs}) are taken out from the voltage measurements at Buses 1 and 4.

Also, for generating the test dataset, 1176 fault cases, different from the training ones, are simulated, considering p-g and positive-to-negative-to-ground (p-n-g) faults with the resistances of 8, 18, 27, 35, 80, and 150 Ω , and with the locations ranged from 1.5% to 98.5% of Line 14 with a 1% step. For each test fault case, the fault signature appearance time, t_0 , and the two input features are derived using the voltage measurements at Buses 1 and 4.

B. Adjusting Parameters and Training

At this stage, for each of single-ended fault locators at Buses 1 and 4, two separate ϵ -SVR estimators are trained for single-pole and double-pole faults, based on the training patterns containing the input features extracted from the locally measured voltages for p-g and p-n fault locations up to a distance of 102 km (i.e., 51% of Line 14) from that bus. The estimators' parameters (i.e., ϵ_{svr} , C_{svr} , and σ_{svr}) are adjusted by a combination of 5-fold cross-validation and Bayesian optimization procedures and presented in Table II.

TABLE II
ADJUSTED PARAMETERS OF THE ϵ -SVR ESTIMATORS

| | Fault locator of Bus 1 | | Fault locator of Bus 4 | |
|------------------|------------------------|-----------------|------------------------|-----------------|
| | For single-pole | For double-pole | For single-pole | For double-pole |
| ϵ_{svr} | 0.0600 | 0.1462 | 0.2559 | 0.5886 |
| C_{svr} | 995.1 | 954.6 | 985.8 | 994.5 |
| σ_{svr} | 0.8171 | 0.6897 | 0.7882 | 0.7677 |

C. Fault-location Results for Unseen Test Cases

In all the 1176 test cases, the faulty half-line and the valid fault-location result have been correctly determined by comparing the fault signature appearance time, t_0 , estimated at Buses 1 and 4. As an example, Fig. 10 represents variations of t_0 obtained at both terminals in terms of the fault distance from Bus 4, for 35- Ω p-g faults at 0.8 s. As is clear in this figure, the values of t_0 obtained at Buses 1 and 4 are smaller for the faults in the corresponding half-lines of their sides, and vice versa.

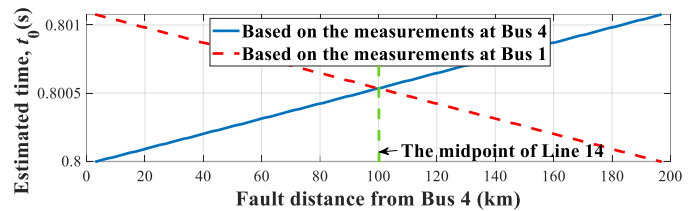


Fig. 10. Variations of the fault signature appearance time estimated at Buses 1 and 4 in terms of the fault location, for 35- Ω p-g faults at 0.8 s.

The fault-location error is computed by dividing the absolute difference of the estimated and actual fault distances by the total line length. Here, given a large number of test cases, the mean and standard deviation of the fault-location percentage errors (i.e., μ_e and σ_e) are considered to evaluate the test performance.

Fig. 11 exhibits μ_e for different fault locations considered in the test conditions. As shown in this figure, the estimation accuracy increases, and μ_e reaches about 0.5% or even less by moving the fault location away from the midpoint and approaching the terminals.

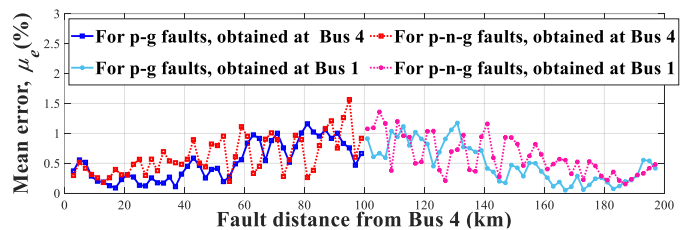


Fig. 11. Mean of estimation errors in terms of the location of faults.

Table III presents the values of μ_e and σ_e for various fault resistances considered in the test conditions. Based on this table, the estimation accuracy is acceptable for different fault resistances. Also, the estimation errors for all the test cases related to p-g and p-n-g faults have the acceptable mean values of 0.516% and 0.624%, respectively. Another significant point in the test results of Table III is the excellent generalizability of the double-pole fault estimators in the face of p-n-g faults, while they were trained based on only p-n faults.

TABLE III
 TEST RESULTS FOR DIFFERENT FAULT RESISTANCES

| | For p-g faults | | For p-n-g faults | |
|--------------------|----------------|----------------|------------------|----------------|
| | μ_e (%) | σ_e (%) | μ_e (%) | σ_e (%) |
| $R_f = 8 \Omega$ | 0.639 | 0.428 | 0.835 | 0.563 |
| $R_f = 18 \Omega$ | 0.635 | 0.616 | 0.782 | 0.631 |
| $R_f = 27 \Omega$ | 0.476 | 0.578 | 0.710 | 0.624 |
| $R_f = 35 \Omega$ | 0.843 | 0.971 | 0.604 | 0.602 |
| $R_f = 80 \Omega$ | 0.283 | 0.205 | 0.520 | 0.471 |
| $R_f = 150 \Omega$ | 0.221 | 0.150 | 0.293 | 0.315 |
| Total | 0.516 | 0.601 | 0.624 | 0.573 |

Extra tests considering fault resistances higher than the training range (i.e., higher than 200 Ω) have revealed that the mean of estimation errors remains below 1% at least up to 350 Ω , in which the mean errors obtained for the p-g and p-n-g faults are 0.674% and 0.472%, respectively.

D. Higher and Lower Sampling Frequencies

The test results for different sampling frequencies, f_s , are provided in Table IV. Based on these results, increasing the sampling frequency to 500 kHz has improved the estimation accuracy, especially for double-pole faults. Conversely, sampling frequency reduction has degraded accuracy. For example, the mean of estimation errors for all the fault types has undesirably reached above 1% at the frequency of 62.5 kHz.

TABLE IV
 TEST RESULTS FOR DIFFERENT SAMPLING FREQUENCIES

| | For p-g faults | | For p-n-g faults | |
|------------------|----------------|----------------|------------------|----------------|
| | μ_e (%) | σ_e (%) | μ_e (%) | σ_e (%) |
| $f_s = 500$ kHz | 0.456 | 0.531 | 0.471 | 0.402 |
| $f_s = 250$ kHz | 0.516 | 0.601 | 0.624 | 0.573 |
| $f_s = 125$ kHz | 0.739 | 1.015 | 1.064 | 1.171 |
| $f_s = 62.5$ kHz | 1.368 | 2.130 | 2.162 | 2.468 |

E. Noisy Measurements

White Gaussian noises with different signal-to-noise ratios (SNRs) are added to the signals measured in the test fault cases, and the features extracted from these noisy signals are presented to the fault-location estimators pretrained with noise-free data. Table V provides the estimation results for different noise levels. Based on this table, the scheme's accuracy is acceptable for SNRs higher than 65 dB.

TABLE V
 TEST RESULTS FOR DIFFERENT SNRS

| | For p-g faults | | For p-n-g faults | |
|-------------------|----------------|----------------|------------------|----------------|
| | μ_e (%) | σ_e (%) | μ_e (%) | σ_e (%) |
| SNR = ∞ dB | 0.516 | 0.601 | 0.624 | 0.573 |
| SNR = 85 dB | 0.557 | 0.657 | 0.677 | 0.614 |
| SNR = 80 dB | 0.591 | 0.720 | 0.688 | 0.643 |
| SNR = 75 dB | 0.675 | 0.832 | 0.761 | 0.752 |
| SNR = 70 dB | 0.762 | 0.983 | 0.881 | 0.929 |
| SNR = 65 dB | 0.875 | 1.219 | 1.058 | 1.207 |
| SNR = 60 dB | 1.046 | 1.520 | 1.386 | 1.698 |
| SNR = 55 dB | 1.753 | 2.607 | 2.104 | 2.526 |

F. Deviations in Line Parameters

All the 1176 test fault cases mentioned in Section V.A are simulated again by changing the pole spacing and installation depth of all the lines in the test grid by -20% relative to the configuration shown in Fig. 3. The mean of estimation errors relative to those obtained with the same line parameters used in the training stage has slightly increased from 0.516% to 0.555% for the p-g faults and from 0.624% to 0.649% for the p-n-g faults. In other words, the estimators can tolerate a reasonable level of deviations in the line parameters.

G. Comparison with Other Fault-Location Methods

Table VI provides a comparison between the proposed fault-location scheme and other ones presented for multiterminal HVDC systems. Apart from the method presented in [17], which is implementable with either one-end or two-end data sampled at a high rate, the proposed scheme is the only method that can estimate the fault location using the local measurements without being affected by communication link noises. Although the proposed scheme requires synchronized timestamping to determine the faulty half-line and select the valid result, in the case of synchronization loss, two fault-location results will be available, one of which will have acceptable accuracy. As shown in Table VI, this scheme requires a lower sampling frequency than the methods presented in [8]-[10], [17].

TABLE VI
 COMPARISON BETWEEN THE PROPOSED AND OTHER SCHEMES

| Principal element | Required measurements | Sampling frequency | Postfault data |
|--------------------------------|--|--------------------|----------------|
| Traveling waves [8]-[10] | Synchronized currents from all converter stations | 1-2 MHz | Not declared |
| Traveling waves [11] | Synchronized currents from sensors distributed along lines | 5-135 kHz | Less than 1 ms |
| Traveling waves [12] | Synchronized currents from sensors distributed along lines | 5 kHz | 5 ms |
| High-frequency components [13] | Synchronized currents from both terminals | 50 kHz | 10 ms |
| High-frequency components [14] | Currents from both terminals | 10 kHz | 10 ms |
| R-L line model [15] | Synchronized currents and voltages from both terminals | 50 kHz | 5 ms |
| Dynamic line model [16] | Synchronized currents and voltages from both terminals | 20 kHz | 5 ms |
| Model traveling-waves [17] | One-end/two-end currents of cables' conducting layers | 1 MHz | Not declared |
| Transient response (proposed) | Local voltage (for calculation at each terminal) | 250 kHz | 2.5 ms |

An algorithm that uses a shorter postfault data window for fault location will be more compatible with the grids protected by quick-action fault-detection algorithms and circuit breakers, owing to the confidence in the availability of its required data before the ultra-fast fault-isolation stage. Compared to the methods developed using a declared length of postfault signals in Table VI, the proposed scheme requires a shorter data window than all the methods, except the method presented in [11]. It is worth mentioning that the algorithm presented in [11] needs synchronized current signals captured via sensors

distributed along lines, which can inflict difficulties and costs in the practical implementation.

VI. CONCLUSION

A scheme has been designed based on useful features extracted from voltage transient responses and a soft computing strategy for fault location in HVDC grids. The designed scheme's performance has been comprehensively evaluated in an HB-MMC-HVDC grid, considering 1176 various test fault cases not seen in the training stage. The overall mean of estimation errors for these test cases was about 0.570%, which authenticates the proposed algorithm's acceptable accuracy and generalization power. The additional test results have also shown that the estimators can tolerate reasonable levels of measurement noises and deviations in the line parameters. The required comparatively short postfault data makes the algorithm more compatible with quick-action fault detectors and circuit breakers. Presenting two probable estimations based on the local measurements, even in the absence of time synchronization, is another salient advantage of this scheme.

REFERENCES

[1] J. Yang, J. E. Fletcher, and J. O. Reilly, "Short-circuit and ground fault analyses and location in VSC-based dc network cables," *IEEE Trans. Ind. Electron.*, vol. 59, no. 10, pp. 3827-3837, Oct. 2012.

[2] S. Du, A. Dekka, B. Wu, and N. Zargari, *Modular Multilevel Converters: Analysis, Control, and Applications*. Hoboken, NJ, USA: Wiley-IEEE Press, 2018.

[3] C. Zhang, G. Song, T. Wang, and L. Yang, "Single-ended traveling wave fault location method in dc transmission line based on wave front information," *IEEE Trans. Power Deliv.*, vol. 34, no. 5, pp. 2028-2038, Oct. 2019.

[4] M. Ashouri, F. F. D. Silva, and C. L. Bak, "On the application of modal transient analysis for online fault localization in HVDC cable bundles," *IEEE Trans. Power Deliv.*, vol. 35, no. 3, pp. 1365-1378, Jun. 2020.

[5] T. Bi, S. Wang, and K. Jia, "Single pole-to-ground fault location method for MMC-HVDC system using active pulse," *IET Gener. Transm. Distrib.*, vol. 12, no. 2, pp. 272-278, Jan. 2018.

[6] X. Zheng, M. H. Nadeem, N. Tai, S. Habib, B. Wang, M. Yu, and Y. He, "A transient current protection and fault location scheme for MMC-HVDC transmission network," *Int. J. Electr. Power Energy Syst.*, vol. 124, Art. no. 106348, Jan. 2021.

[7] Q. Huai, L. Qin, K. Liu, H. Ding, X. Liao, and T. Tan, "Combined line fault location method for MMC-HVDC transmission systems," *IEEE Access*, vol. 8, pp. 170794-170806, 2020.

[8] O. M. K. K. Nanayakkara, A. D. Rajapakse, and R. Wachal, "Traveling-wave-based line fault location in star-connected multiterminal HVDC systems," *IEEE Trans. Power Deliv.*, vol. 27, no. 4, pp. 2286-2294, Oct. 2012.

[9] S. Azizi, M. Sanaye-Pasand, M. Abedini, and A. Hasani, "A traveling-wave-based methodology for wide-area fault location in multiterminal dc systems," *IEEE Trans. Power Deliv.*, vol. 29, no. 6, pp. 2552-2560, Dec. 2014.

[10] S. Azizi, S. Afsharnia, and M. Sanaye-Pasand, "Fault location on multi-terminal dc systems using synchronized current measurements," *Int. J. Electr. Power Energy Syst.*, vol. 63, pp. 779-786, Dec. 2014.

[11] D. Tzelepis, G. Fusiek, A. Dyško, P. Niewczas, C. Booth, and X. Dong, "Novel fault location in MTDC grids with non-homogeneous transmission lines utilizing distributed current sensing technology," *IEEE Trans. Smart Grid*, vol. 9, no. 5, pp. 5432-5443, Sep. 2018.

[12] D. Tzelepis, A. Dyško, G. Fusiek, P. Niewczas, S. Mirsaeidi, C. Booth, and X. Dong, "Advanced fault location in MTDC networks utilizing optically-multiplexed current measurements and machine

learning approach," *Int. J. Electr. Power Energy Syst.*, vol. 97, pp. 319-333, Apr. 2018.

[13] X. Zhang, N. Tai, Y. Wang, and J. Liu, "EMTR-based fault location for dc line in VSC-MTDC system using high-frequency currents," *IET Gener. Transm. Distrib.*, vol. 11, no. 10, pp. 2499-2507, Jul. 2017.

[14] J. Li, Q. Yang, H. Mu, S. Le Blond, and H. He, "A new fault detection and fault location method for multi-terminal high voltage direct current of offshore wind farm," *Appl. Energy*, vol. 220, pp. 13-20, Jun. 2018.

[15] J. Xu, L. Y. C. Zhao, and J. Liang, "A model based dc fault location scheme for multi-terminal MMC-HVDC systems using a simplified transmission line representation," *IEEE Trans. Power Deliv.*, vol. 35, no. 1, pp. 386-395, Feb. 2020.

[16] B. Wang, Y. Liu, D. Lu, K. Yue, and R. Fan, "Transmission line fault location in MMC-HVDC grids based on dynamic state estimation and gradient descent," *IEEE Trans. Power Deliv.*, 2020. DOI: 10.1109/TPWRD.2020.3013755

[17] M. Ashouri, F. F. d. Silva, C. L. Bak, A. Abdoos, and S. M. Hosseini, "Modal online differential fault detection and localisation scheme for VSC-MTDC cable transmission," *IET Gener. Transm. Distrib.*, vol. 14, no. 20, pp. 4475-4487, Oct. 2020.

[18] Y. Wang, W. Wen, C. Zhang, Z. Chen, and C. Wang, "Reactor sizing criterion for the continuous operation of meshed HB-MMC-based MTDC system under dc faults," *IEEE Trans. Ind. Appl.*, vol. 54, no. 5, pp. 5408-5416, Sep.-Oct. 2018.

[19] N. Tong, X. Lin, Y. Li, Z. Hu, N. Jin, F. Wei, and Z. Li, "Local measurement-based ultra-high-speed main protection for long distance VSC-MTDC," *IEEE Trans. Power Deliv.*, vol. 34, no. 1, pp. 353-364, Feb. 2019.

[20] W. Leterme, J. Beerten, and D. V. Hertem, "Equivalent circuit for half-bridge MMC dc fault current contribution," in *IEEE Int. Energy Conf. (ENERGYCON)*, Leuven, Belgium, 2016, pp. 1-6.

[21] W. Leterme, N. Ahmed, J. Beerten, L. Ångquist, D. V. Hertem, and S. Norrga, "A new HVDC grid test system for HVDC grid dynamics and protection studies in EMT-type software," in *11th IET Int. Conf. AC DC Power Transm.*, Birmingham, UK, 2015, pp. 1-7.

[22] F. Golnaraghi and B. C. Kuo, *Automatic Control Systems*, 9th ed. Hoboken, NJ, USA: Wiley, 2009.

[23] Q. Huang, G. Zou, X. Wei, C. Sun, and H. Gao, "A non-unit line protection scheme for MMC-based multi-terminal HVDC grid," *Int. J. Electr. Power Energy Syst.*, vol. 107, pp. 1-9, May 2019.

[24] Y. Song, J. Sun, M. Saeedifard, S. Ji, L. Zhu, and A. P. S. Meliopoulos, "Optimum selection of circuit breaker parameters based on analytical calculation of overcurrent and overvoltage in multiterminal HVDC grids," *IEEE Trans. Ind. Electron.*, vol. 67, no. 5, pp. 4133-4143, May 2020.

[25] J. Hu, K. Xu, L. Lin, and R. Zeng, "Analysis and enhanced control of hybrid-MMC-based HVDC systems during asymmetrical dc voltage faults," *IEEE Trans. Power Deliv.*, vol. 32, no. 3, pp. 1394-1403, Jun. 2017.

[26] W. Leterme, P. Tielens, S. D. Boeck, and D. V. Hertem, "Overview of grounding and configuration options for meshed HVDC grids," *IEEE Trans. Power Deliv.*, vol. 29, no. 6, pp. 2467-2475, Dec. 2014.

[27] *MATLAB User's Guide: R2018b Documentation*, MathWorks Inc, Natick, MA, USA, 2018.

[28] B. Schölkopf and A. J. Smola, *Learning with Kernels: Support Vector Machines, Regularization, Optimization, and Beyond*. Cambridge, MA, USA: MIT Press, 2001.



Mohammad Farshad was born in Gonbad Kavous, Iran, in 1981. He received the B.Sc. degree in power transmission and distribution networks engineering from the Power and Water University of Technology (PWUT), Tehran, Iran, in 2003, and the M.Sc. and Ph.D. degrees in power system engineering from the Ferdowsi University of Mashhad, Mashhad, Iran, in 2006 and 2013, respectively.

He is currently an Assistant Professor in the Department of Electrical Engineering, Faculty of Basic Sciences and Engineering, Gonbad Kavous University. His main research interest is the application of intelligent systems in power system protection, operation, and planning.